What is the final size of turbulent mixing zones driven by the Faraday instability?

B.-J. Gréa[1],† and A. Ebo Adou[2]

[1]CEA, DAM, DIF, F-91297 Arpajon, France

[2]CMLA, ENS Cachan, France

Miscible fluids of different densities subjected to strong time-periodic accelerations normal to their interface can mix due to Faraday instability effects. Turbulent fluctuations generated by this mechanism lead to the emergence and the growth of a mixing layer. Its enlargement is gradually slowed down as the resonance conditions driving the instability cease to be fulfilled. The final state corresponds to a saturated mixing zone in which the turbulence intensity progressively decays. A new formalism based on second-order correlation spectra for the turbulent quantities is introduced for this problem. This method allows for the prediction of the final mixing zone size and extends results from classical stability analysis limited to weakly nonlinear regimes. We perform at various forcing frequencies and amplitudes a large set of homogeneous and inhomogeneous numerical simulations, extensively exploring the influence of initial conditions. The mixing zone widths, measured at the end of the simulations, are satisfactorily compared to the predictions, and bring a strong support to the proposed theory. The flow dynamics is also studied and reveals the presence of sub-harmonic as well as harmonic modes depending on the initial parameters in the Mathieu phase diagram. Important changes in the flow anisotropy, corresponding to the large scale structures of turbulence, occur. This phenomenon appears directly related to the orientation of the most amplified gravity waves excited in the system, evolving due to the enlargement of the mixing zone.

Key words: buoyancy-driven instability, stratified turbulence, turbulent mixing

1. Introduction

The interface between two fluids of densities $\rho_1 > \rho_2$ may destabilize due to the Faraday instability (Faraday 1831; Miles & Henderson 1990) when a time-periodic acceleration is applied perpendicular to it. In the simplest case of a single-frequency acceleration,

$$G(t) = G_0(1 + F\cos\omega t), \tag{1.1}$$

the system is excited by different harmonic or sub-harmonic resonances determined by the mean acceleration G_0, the frequency ω and the amplitude F of oscillations.

† Email address for correspondence: benoit-joseph.grea@cea.fr

Due to its importance, the literature on the Faraday problem is vast and diversified. Many studies focus on the instability onset and try to understand pattern formation. The system is indeed well known for producing fascinating structures observed in many experiments (Simonelli & Gollub 1989; Edwards & Fauve 1994; Kudrolli & Gollub 1996; Binks & van de Water 1997; Arbell & Fineberg 2002). In the latter, multiple-frequency forcing is often considered, enhancing the richness of the solutions.

The linear theory of the Faraday instability relies on Floquet analysis and provides the growth rate of interface defaults and dominant wavenumbers. Its inviscid and viscid formulation can be found in Benjamin & Ursell (1954) and Kumar & Tuckerman (1994) respectively. Weakly nonlinear theories such as in Müller (1994), Zhang & Viñals (1997), Chen & Viñals (1999), Skeldon & Guidoboni (2007) derive the amplitude equations for interface waves. These results successfully explain pattern formation in many Faraday experiments, particularly in large containers with moderate viscosity (Skeldon & Rucklidge 2015).

Other regimes deserve to be studied in the Faraday problem. When the fluids are miscible (see Zoueshtiagh, Amiroudine & Narayanan 2009, Diwakar *et al.* 2015), when the forcing amplitude is strong enough (Gollub & Ramshankar 1991; Bosch & van de Water 1993) or for sufficiently disordered initial conditions, standing waves progressively disorganize and interact with each other. Their energy begins to be distributed among a continuous spectrum. The flow becomes turbulent and sees the emergence of a mixing zone. In this case, a deterministic approach is difficult to use but one can turn to averaging methods (see Gaponenko *et al.* (2015) in a similar context) as in classical turbulence theory. However, the problem of the Faraday instability in the turbulent regime has never been addressed from a theoretical point of view.

In order to shed light on the dynamics of the mixing layer driven by the Faraday instability, a possible strategy consists first in analysing how the mean density gradient interacts with turbulence. This approach, initiated by Hunt & Carruthers (1990), Hanazaki & Hunt (1996), Nazarenko, Kevlahan & Dubrulle (1999), takes exactly into account the buoyancy production of kinetic energy and rapid pressure effects which have a central role in the problem. However, it neglects the dissipation and the energy transfers accounting for the interaction between turbulence with itself. Despite this limitation, this procedure has proved useful for instance to predict the growth rates of turbulent mixing zone driven by the Rayleigh–Taylor instability when considering the nonlinear coupling between turbulence and the mean density gradient (Gréa 2013). Can this methodology also be relevant for turbulent mixing zones driven by Faraday instabilities?

Accordingly, it is important to identify the parameters controlling the turbulence production. In stratified media, the energy transferred to flow fluctuations is carried by gravity internal waves characterized by the buoyancy (or Brunt–Väisälä) frequency:

$$N = \left(\frac{2\mathcal{A}G_0}{L}\right)^{1/2}. \tag{1.2}$$

Here, $\mathcal{A} = (\rho_1 - \rho_2)/(\rho_1 + \rho_2)$ is the Atwood number expressing the contrast of density between the two fluids and $L(t)$ the mixing zone width. In the small Atwood number limit, $2\mathcal{A}/L$ gives the renormalized mean density gradient. Although often introduced in the homogeneous context, this definition of N also corresponds to the maximum frequency in the dispersion relationship for an inhomogeneous mixing zone (see Batchelor & Nitsche 1991, Soulard, Griffond & Gréa 2015) when viscosity and

diffusion are negligible. The parametric instability in a frozen stratification, or constant N has been well evidenced by Benielli & Sommeria (1998) for instance. However, in cases where the mixing zone is allowed to evolve freely, the problem is complicated as the instability implies a growth of L and a diminution of the buoyancy frequency N. For a single-frequency forcing, no resonance conditions are possible if $N \ll \omega$. Therefore, the instability is expected to vanish after some time, causing a saturation of the mixing zone accompanied by a decay of the turbulence intensity. This scenario has been confirmed experimentally and numerically in Zoueshtiagh *et al.* (2009) and Amiroudine, Zoueshtiagh & Narayanan (2012). The growth rates and characteristic length scales corresponding to the instability onset have been thoroughly analysed in these studies. We would like to pursue this analysis by determining the final size L_{sat} of mixing zones driven by the Faraday instability.

Determining L_{sat}, although interesting from a theoretical point of view, is also of practical importance as it opens a path to a possible control of mixing zone sizes. For instance, the Faraday instability is already used to generate small perturbations at the interface between fluids for initial conditions in shock tube experiments as in Jacobs *et al.* (2013). One can imagine generating different initial conditions by creating saturated mixing zones before making them interact with a shock wave. Therefore, while most studies on Faraday waves focus on the initial stage, we propose to investigate its termination after reaching a turbulent state.

As always, dimensional analysis is the first step to study a problem in fluid mechanics. Assuming that the saturated mixing zone size does not depend at leading order on the initial conditions and the dissipative processes induced by viscosity or molecular diffusion, then we should have

$$L_{sat} = \frac{2\mathcal{A}G_0}{\omega^2}\mathcal{G}(F), \tag{1.3}$$

with $\mathcal{G}$ an unknown function of the amplitude F of the imposed oscillations. The main objective of this work is therefore to check the validity of (1.3) and to propose an expression for the function $\mathcal{G}$ from various stability and turbulence theory arguments.

This paper is organized as follows. In §2 we detail the basic equations and the theoretical framework of the study. In §3 we analyse a nonlinear model which reproduces the inner mechanism of the instability and derive a saturation criterion. In §4 we present the numerical simulations and discuss the results.

2. Basic equations

We propose different frameworks to study turbulent mixing zones driven by time-varying accelerations. Among other properties, turbulent mixing zones are highly nonlinear, inhomogeneous, anisotropic and dissipative systems. It is worthwhile to perform some simplifications to extract important physical ingredients. First, we recall the complete set of equations expressing the dynamics of mixing zones in the limit of small Atwood numbers. Then, a homogeneous system for turbulent fluctuations is considered by assuming an uniform density gradient. Finally, we introduce a model for second-order correlations which retain the nonlinear coupling between the mean density gradient and turbulent quantities.

2.1. *Equations for the mixing zone (MZ)*

We consider an incompressible mixing layer between two miscible fluids. We assume the density of the mixture depends linearly on the mass concentration of heavy fluid

$C(\boldsymbol{x}, t) \in [0\ 1]$ with $\boldsymbol{x}$ the position and t the time. This system is governed by the classical Boussinesq/Navier–Stokes equations for $C(\boldsymbol{x}, t)$ and the velocity $\boldsymbol{U}(\boldsymbol{x}, t)$:

$$\partial_t C + (\boldsymbol{U} \cdot \boldsymbol{\nabla})C = \mathcal{D}\Delta C, \qquad (2.1a)$$

$$\partial_t \boldsymbol{U} + (\boldsymbol{U} \cdot \boldsymbol{\nabla})\boldsymbol{U} = -\boldsymbol{\nabla}P + 2\mathcal{A}CG(t)\boldsymbol{n}_3 + \mu\Delta\boldsymbol{U}, \qquad (2.1b)$$

$$\boldsymbol{\nabla} \cdot \boldsymbol{U} = 0, \qquad (2.1c)$$

where in (2.1*a,b*), $P(\boldsymbol{x}, t)$ is the reduced pressure, μ the viscosity, $\boldsymbol{n}_3$ the normalized vertical vector and $\mathcal{D}$ the diffusion coefficient.

The position $\boldsymbol{x}$ is expressed in the usual Cartesian frame with the vertical direction corresponding to the acceleration vector identified by the suffix $_3$. In this problem, quantities are assumed statistically invariant in the horizontal plane (homogeneity) as we do not consider boundary conditions. A quantity, say for example $Q(\boldsymbol{x}, t)$, is averaged along the horizontal as follows:

$$\langle Q \rangle_H(x_3, t) = \lim_{\ell \to +\infty} \frac{1}{\ell^2} \int_{-\ell/2}^{+\ell/2} \int_{-\ell/2}^{+\ell/2} Q(\boldsymbol{x}, t)\, \mathrm{d}x_1\, \mathrm{d}x_2. \qquad (2.2)$$

We introduce the Reynolds decomposition separating the quantity Q between the mean $\langle Q \rangle_H$ and its fluctuating part q as

$$Q = \langle Q \rangle_H + q, \qquad (2.3)$$

with $\langle q \rangle_H = 0$.

In this context, the equations for the fluctuating velocity $\boldsymbol{u}(\boldsymbol{x}, t)$ and concentration $c(\boldsymbol{x}, t)$ deduced from (2.1*a–c*) are

$$\partial_t c + (\boldsymbol{u} \cdot \boldsymbol{\nabla})c = -\partial_3\langle C \rangle_H u_3 + \mathcal{D}\Delta c, \qquad (2.4a)$$

$$\partial_t \boldsymbol{u} + (\boldsymbol{u} \cdot \boldsymbol{\nabla})\boldsymbol{u} = -\boldsymbol{\nabla}p + 2\mathcal{A}cG(t)\boldsymbol{n}_3 + \mu\Delta\boldsymbol{u}, \qquad (2.4b)$$

$$\boldsymbol{\nabla} \cdot \boldsymbol{u} = 0, \qquad (2.4c)$$

with $p(\boldsymbol{x}, t)$ the fluctuating reduced pressure. Note that the mean velocity is zero $\langle \boldsymbol{U} \rangle_H = 0$ and as also by definition fluctuating quantities $\langle \boldsymbol{u} \rangle_H = \langle c \rangle_H = \langle p \rangle_H = 0$. In addition, the dynamical equation for the mean concentration profile $\langle C \rangle_H$, neglecting molecular diffusion, is provided by

$$\partial_t \langle C \rangle_H = -\partial_3 \langle u_3 c \rangle_H. \qquad (2.4d)$$

The closed system of equations (2.4*a–d*) determines the dynamics of a mixing zone driven by an acceleration. Note that for constant positive acceleration $G_0 > 0$, the stratification is stable if $\partial_3\langle C \rangle_H > 0$ and unstable for $\partial_3\langle C \rangle_H < 0$.

We define the mixing zone width classically from the mean concentration profile as in Andrews & Spalding (1990):

$$L = 6 \int_{-\infty}^{+\infty} \langle C \rangle_H(1 - \langle C \rangle_H)\, \mathrm{d}x_3. \qquad (2.5)$$

The pre-factor in (2.5) is chosen such that it gives the exactly the width for a linear density (concentration) profile inside the mixing zone.

If we assume that the mean concentration remains linear inside the mixing zone and uniform equal to 0 or 1 outside, an equation for the mixing zone width can be derived from (2.4*d*), (2.5) (see also Gréa 2013) leading to

$$\dot{L} = \frac{12}{L} \int_{-\infty}^{+\infty} \langle u_3 c \rangle_H\, \mathrm{d}x_3. \qquad (2.6)$$

2.2. *The stratified homogeneous turbulence (SHT) model*

In order to analyse the mechanisms controlling buoyancy-driven turbulence, we consider a simplified problem in place of system equations (2.4*a–d*). To this purpose, varied idealized models have been previously introduced relying on homogeneity assumptions for the turbulent quantities (see for instance Batchelor, Canuto & Chasnov (1992), Livescu & Ristorcelli (2007), Chung & Pullin (2010) or Burlot *et al.* (2015)).

The latter one, addressed to stratified homogeneous turbulence (SHT) model, considers a uniform mean concentration gradient ($\partial_3 \langle C \rangle_H = -1/L$) leading to

$$\partial_t c + (\boldsymbol{u} \cdot \boldsymbol{\nabla}) c = \frac{1}{L} u_3 + \mathcal{D} \Delta c, \tag{2.7a}$$

$$\partial_t \boldsymbol{u} + (\boldsymbol{u} \cdot \boldsymbol{\nabla}) \boldsymbol{u} = -\boldsymbol{\nabla} p + 2 \mathcal{A} c G(t) \boldsymbol{n}_3 + \mu \Delta \boldsymbol{u}, \tag{2.7b}$$

$$\boldsymbol{\nabla} \cdot \boldsymbol{u} = 0, \tag{2.7c}$$

where the ensemble averages satisfy $\langle \boldsymbol{u} \rangle = \langle c \rangle = 0$. In this flow, averaged quantities do not depend on the position vector $\boldsymbol{x}$ due to homogeneity.

In order to complete the system and to mimic the evolution of the mean density gradient, an equation for the mixing zone width must be added. A possible choice, directly inspired by (2.6), is

$$\dot{L} = \frac{12}{L} \ell_0 \langle u_3 c \rangle, \tag{2.7d}$$

where ℓ_0 is an arbitrary characteristic length introduced for dimensional purposes such that $\ell_0 \langle u_3 c \rangle$ represents the concentration flux integrated along the mixing zone. Other choices are possible, such as for instance $\ell_0 \sim L$ (Griffond, Gréa & Soulard 2014). The difference between the two versions relies in the interpretation of results with respect to the inhomogeneous problem. For instance, the choice in this work is $\ell_0 = 1$ in (2.7*d*), so that the second-order correlations scale as integrated quantities along the mixing zone while with $\ell_0 \sim L$ they scale as turbulent quantities in the middle of the mixing zone.

It should be stated clearly that the SHT model, although sharing many properties with the complete inhomogeneous problem, cannot be viewed as an approximation of it. Note that the decoupling between turbulent quantities and the mixing width in SHT is advantageous for simulations as will be seen in § 4.1.

2.3. *The rapid acceleration (RA) model*

In the context of the SHT framework, we can define the various turbulent spectra as Fourier transforms of two-point correlations: see for instance Burlot *et al.* (2015). Due to axisymmetry, these spectra depend only on the wave modulus k and the angle θ between the vertical $\boldsymbol{n}_3$ and the wave vector $\boldsymbol{k}$. We can further introduce k-integrated spectra for the vertical velocity $\mathcal{E}_{u_3 u_3}$, the concentration $\mathcal{E}_{cc}$ and the concentration flux $\mathcal{E}_{u_3 c}$ which depend on θ only and are related to one-point correlations as follows:

$$\langle u_3 u_3 \rangle = \int_0^\pi \mathcal{E}_{u_3 u_3} \sin(\theta) \, \mathrm{d}\theta, \quad \langle cc \rangle = \int_0^\pi \mathcal{E}_{cc} \sin(\theta) \, \mathrm{d}\theta, \quad \langle u_3 c \rangle = \int_0^\pi \mathcal{E}_{u_3 c} \sin(\theta) \, \mathrm{d}\theta. \tag{2.8a-c}$$

From (2.7*a–c*) and following the same procedure as in Gréa (2013), it is possible to express simply the dynamics of integrated spectra by neglecting nonlinear and viscous/diffusive terms, retaining only the effects of buoyancy and pressure:

$$\partial_t \mathcal{E}_{u_3 c} = \frac{1}{L}\mathcal{E}_{u_3 u_3} - 2\mathcal{A}G(t)\sin^2(\theta)\mathcal{E}_{cc}, \qquad (2.9a)$$

$$\partial_t \mathcal{E}_{u_3 u_3} = -4\mathcal{A}G(t)\sin^2(\theta)\mathcal{E}_{u_3 c}, \qquad (2.9b)$$

$$\partial_t \mathcal{E}_{cc} = \frac{2}{L}\mathcal{E}_{u_3 c}, \qquad (2.9c)$$

$$\dot{L} = \frac{12}{L}\int_0^\pi \mathcal{E}_{u_3 c}\sin(\theta)\,\mathrm{d}\theta. \qquad (2.9d)$$

The nonlinearity remaining in the system of equations (2.9a–d) is due to the evolution of the mixing zone width L. Otherwise the system describes classically the dynamics of gravity waves. In practice, this approach is valid only when the acceleration is strong compared to the inertia of turbulent structures and lasts only for a short period of time before nonlinear terms coupling the turbulent fluctuation modes recover their intensity. This statistical approach for integrated spectra described by (2.9a–d) can be referred to as the rapid acceleration (RA) model. It has also been introduced in the context of inhomogeneous mixing zones for Rayleigh–Taylor instability in Gréa (2013).

At this stage, we make an assumption in order to reduce the RA model for the evolving mixing zone into a single differential equation. If the fluctuating concentration c and vertical velocity u_3 are initially correlated, implying $\mathcal{E}_{u_3 c}^2 = \mathcal{E}_{u_3 u_3}\mathcal{E}_{cc}$, it can be easily shown from the RA equations that it remains correlated for all t. In this case, it is possible to simplify the system by introducing $\mathcal{U}(t,\theta) = \mathcal{E}_{u_3 u_3}^{1/2}(t,\theta)$ and $\mathcal{B}(t,\theta) = \mathcal{E}_{cc}^{1/2}(t,\theta)$, leading to

$$\partial_t \mathcal{U} = -2\mathcal{A}G(t)\sin^2(\theta)\mathcal{B}, \qquad (2.10a)$$

$$\partial_t \mathcal{B} = \frac{1}{L}\mathcal{U}, \qquad (2.10b)$$

$$\dot{L} = \frac{12}{L}\int_0^\pi \mathcal{U}\mathcal{B}\sin(\theta)\,\mathrm{d}\theta. \qquad (2.10c)$$

Alternatively, it may be noted that the system can be expressed in the form of a nonlinear second-order equation for $\mathcal{B}$, as the equation for L can be integrated:

$$\partial_{tt}\mathcal{B}(t,\theta) + \frac{\dot{L}(t)}{L(t)}\partial_t \mathcal{B}(t,\theta) + \frac{2\mathcal{A}G(t)\sin^2(\theta)}{L(t)}\mathcal{B}(t,\theta) = 0, \qquad (2.11a)$$

$$L(t) = 6\int_0^\pi \mathcal{B}^2(t,\theta)\sin(\theta)\,\mathrm{d}\theta + L_0, \qquad (2.11b)$$

where L_0 in (2.10c) is the integration constant depending on initial conditions. Without loss of generality, the system can be written in a non-dimensional form using the new variables $B(t',\theta) = \mathcal{B}(t,\theta)/(6L_0)^{1/2}$ and $t' = N_0 t$ with $N_0 = (2\mathcal{A}G_0/L_0)^{1/2}$ and considering the time-periodic acceleration equation (1.1). For simplicity, we take t for the non-dimensional time in place of t'. This gives the system of equations

$$\partial_{tt}B(t,\theta) - 2\frac{\dot{\Omega}(t)}{\Omega(t)}\partial_t B(t,\theta) + \sin^2(\theta)\Omega^2(t)(1 + F\cos(\omega/N_0 t))B(t,\theta) = 0, \quad (2.12a)$$

$$\Omega^2(t) = \frac{1}{1 + \displaystyle\int_0^\pi B^2(t,\theta)\sin(\theta)\,\mathrm{d}\theta}. \qquad (2.12b)$$

We shall now use this reduced system of equations (2.12a,b) in order to find the final states of the mixing zone driven by the Faraday instability.
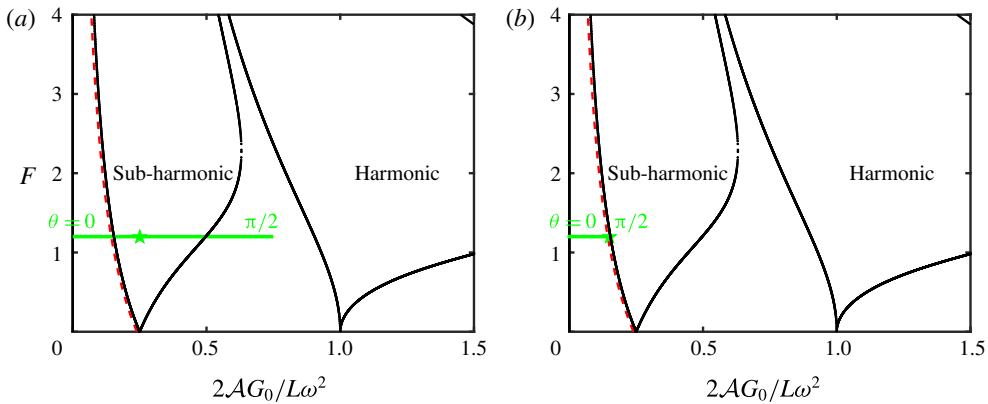
FIGURE 1. (Colour online) Stability diagram of the Mathieu equation as a function of ratio of frequency N^2/ω^2 and amplitude of forcing F. Harmonic and sub-harmonic unstable regions are shown. Green solid line: frequencies excited in the RA model corresponding to the different orientation angles θ of gravity waves. The two graphs show the situation (*a*) at an initial time and (*b*) at a later time after the growth and saturation of L due to the parametric instability. Green star: modes corresponding to the maximum growth rate of the instability. Red dashed line: neutral curve corresponding to the expected saturation width of the mixing zone.

3. Dynamics of mixing zones under parametric forcing

We present in this section the principal arguments leading to the prediction of the mixing zone saturation width. To this end, we perform a linear stability analysis and propose a multiple time scale expansion of the RA model. The results are then assessed by numerical integration of the RA equations.

3.1. *Linear analysis*

For a specified initial mixing zone width L_0, or equivalently an initial frequency N_0, the RA model has a trivial solution corresponding to $B(t, \theta) = \partial_t B(t, \theta) = 0$. The linear equation for the fluctuations around this state can be simply obtained by replacing $\Omega = 1$ and $\dot{\Omega} = 0$ in (2.12a). This gives an infinite set of decoupled Mathieu oscillators parametrized by the orientation angle $\theta \in [0 \ \pi/2]$, which are further characterized by the continuous frequency $\sin(\theta)$.

The instability zones for each oscillators are associated with the classical resonance conditions $n\omega/2 = N_0 \sin \theta \ (\forall n \text{ integer})$. For instance, a sub-harmonic instability is triggered for $n = 1$ while $n = 2$ corresponds to the harmonic case. The instability regions in the $((N_0/\omega)^2, F)$-plane, the Mathieu stability diagram, are the well-known instability tongues and their boundaries the transition curves as shown in figure 1. In practice, the instability zones are obtained numerically following the method described in Kumar & Tuckerman (1994). The linear problem is always stable if the entire segment $[0, (N_0/\omega)^2]$ lies inside the stable region. Otherwise, if at least one angle θ or $(N_0 \sin \theta/\omega^2)^2$ lies inside the unstable region, then linear analysis shows there would be a growth of B and hence the mixing zone.

From this, one can easily deduce the following sufficient condition for instability:

$$\left(\frac{\omega}{N_0}\right)^2 < \mathcal{G}(F), \tag{3.1}$$

where $\mathcal{G}$ indicates the first resonance boundary region triggering parametric growth of B. This suggests the following scenario: as long as there is instability for some angles θ, the mixing zone will enlarge, reducing the buoyancy frequency $N(t)$. We can expect saturation when condition (3.1) is no longer fulfilled, i.e.

$$\left(\frac{\omega}{N_{sat}}\right)^2 = \mathcal{G}(F) \quad \text{or} \quad L_{sat} = \frac{2\mathcal{A}G_0}{\omega^2}\mathcal{G}(F). \tag{3.2a,b}$$

The dynamics of the instability is also governed by angles corresponding to maximum growth rates, not necessarily $\theta = \pi/2$ as indicated in figure 1. It is interesting to note that if $(N/\omega)^2$ is large enough, then both harmonic and sub-harmonic instabilities can be triggered at the same time but for different angles (see §4.2). If initially $(\omega/N_0)^2 \geqslant \mathcal{G}(F)$, the instability is not triggered.

Let us call (3.2) the saturation criterion, and the main objective of this work is to verify its validity. Indeed nonlinear effects corresponding to the evolution of L need also to be considered in the analysis.

3.2. *Perturbation analysis*

The aim of this section is to confirm the validity of the saturation criterion (3.2) even by taking into account weakly nonlinear effects. We use a classical multiple time scale analysis (see Bender & Orszag 1978, Godrèche & Manneville 2005) to find a perturbation expansion of the RA model solutions. These techniques are also used to find transition curves of the Mathieu equation under small forcing or to study weakly nonlinear oscillators.

In order to solve (2.12a,b), we propose the following expansion for B:

$$B(t, \theta) = \varepsilon(B^{(0)}(t, \tau, \theta) + \varepsilon B^{(1)}(t, \tau, \theta) + \varepsilon^2 B^{(2)}(t, \tau, \theta) + \varepsilon^3 B^{(3)}(t, \tau, \theta) + \cdots). \tag{3.3}$$

Here, ε expresses the fact that the perturbation B is small so we can perform a weakly nonlinear analysis. We introduce the slow time variable $\tau = \varepsilon^2 t$. This choice differs from multiple scale analysis of the Mathieu equation and comes from the fact that we approximate the integral over θ in (2.12b) by a stationary phase expansion.

The multiple scale expansion of (2.12a,b) without parametric forcing ($F = 0$) is not detailed here but given in appendix A to lighten this section. Let us give a short summary of the principal results of this analysis. At leading order, the nonlinear terms introduce a phase shift but do not modify the oscillation amplitude. At next order, the amplitudes for B are modified, giving finite amplitude oscillations for L. However, we shall see below that the leading order is sufficient to take into account parametric effects.

For the parametric forcing analysis, we assume further that the natural frequency of the system corresponding to $\theta = \pi/2$ is close to the first resonance condition and that the forcing amplitude is small. This can be written as

$$N_0^2/\omega^2 - 1/4 = \varepsilon^2 \Delta \quad \text{and} \quad F = \varepsilon^2 f \tag{3.4a,b}$$

introducing Δ and f as the detuning and the forcing amplitude parameter, respectively. In appendix A, it is shown that the nonlinear effects appear at order ε^3 for the natural frequency $\Omega^2(t)$ and at order ε^4 for the damping term $-2\dot{\Omega}(t)/\Omega(t)$ (see (A 1), (A 7)).

Reintroducing the different expansions in (2.12a) gives the homogeneous equations for the first two leading orders,

$$\partial_{tt}B^{(0)}(t, \tau, \theta) + \sin^2(\theta)B^{(0)}(t, \tau, \theta) = 0 \quad \text{at order } \varepsilon, \qquad (3.5a)$$

$$\partial_{tt}B^{(1)}(t, \tau, \theta) + \sin^2(\theta)B^{(1)}(t, \tau, \theta) = 0 \quad \text{at order } \varepsilon^2, \qquad (3.5b)$$

with their solutions given by

$$B^{(0)}(t, \tau, \theta) = a(\tau, \theta)e^{i\sin(\theta)t} + a^*(\tau, \theta)e^{-i\sin(\theta)t}, \qquad (3.6a)$$

$$B^{(1)}(t, \tau, \theta) = b(\tau, \theta)e^{i\sin(\theta)t} + b^*(\tau, \theta)e^{-i\sin(\theta)t}. \qquad (3.6b)$$

The leading-order solution $B^{(0)}(t, \tau, \theta)$ allows us to determine the mixing zone width evolution at order ε^2:

$$\frac{L(t)}{L_0} = \frac{1}{\Omega^2(t)} = 1 + 2\varepsilon^2\Lambda(\tau) + O(\varepsilon^3), \qquad (3.7)$$

with $\Lambda(\tau) = \int_0^{+\pi} |a(\tau, \theta)|^2 \sin\theta \, d\theta$. In (3.7), the integral over θ of the oscillating terms $a^2(\tau, \theta)e^{2i\sin(\theta)t}$ and $a^{*2}(\tau, \theta)e^{-2i\sin(\theta)t}$ does not contribute to the leading order of the expansion due to the stationary phase approximation and are postponed to order ε^3.

At order ε^3 in (2.12a), we have

$$\partial_{tt}B^{(2)} + \sin^2(\theta)B^{(2)} = -2\partial_{t\tau}B^{(0)} + 2\sin^2\theta B^{(0)}\Lambda(\tau) - f\sin^2\theta B^{(0)}\sin(\omega/N_0 t). \quad (3.8)$$

Classically, the equation for the amplitudes $a(\tau, \theta)$ in multiple scale analysis are obtained by cancelling secular terms in (3.8). Let us focus on the angle $\theta = \pi/2$ for the leading-order equation (3.6a):

$$-2i\partial_\tau a(\tau) + 2a(\tau)\Lambda(\tau) - \tfrac{1}{2}fa^*(\tau)e^{-4i\Delta\tau} = 0, \qquad (3.9)$$

where the damping still does not appear.

We pose $a(\tau) = g(\tau)e^{-2i\Delta\tau}$ to render the system autonomous which leads to

$$\partial_\tau g(\tau) = i(2\Delta - \Lambda(\tau))g(\tau) - i\frac{f}{4}g^*(\tau). \qquad (3.10)$$

Separating modulus and phase of $g = R(\tau)e^{i\alpha(\tau)}$ leads to

$$\partial_\tau R(\tau) = -\frac{f}{4}R\sin(2\alpha), \qquad (3.11a)$$

$$\partial_\tau \alpha(\tau) = 2\Delta - \Lambda + \frac{f}{4}\cos(2\alpha). \qquad (3.11b)$$

Stationary solutions are $R = 0$ or $2\Delta - \Lambda \pm f/4 = 0$ with $\cos(2\alpha) = 1$; this is very similar to the classical bifurcation diagram of a nonlinear parametric oscillator. The branch $R = 0$ is unstable if the amplitude is large enough, i.e. $f/4 > 2|\Delta|$. In this case the parametric instability is triggered and will saturate at one branch of the solution corresponding to

$$\Lambda = 2\Delta + \frac{f}{4}. \qquad (3.12)$$

Equation (3.12) is what we seek. Using that $L/L_0 = 1 + 2\varepsilon^2\Lambda$ and $(N_0^2/\omega^2) - (1/4) = \varepsilon^2\Delta$, we obtain easily at leading order:

$$\frac{L_{sat}}{L_0} = \frac{N_0^2}{\omega^2}(2F + 4). \qquad (3.13)$$

The relation equation (3.13) is equivalent to the criterion of equation (3.2); in the limit of small forcing the first transition curve corresponds in this case to $\mathcal{G}(F) = 2F + 4$.

In conclusion for this part, we have proved by perturbation analysis the validity of the saturation criterion equation (3.2) under the conditions of small forcing and initial perturbation and if the natural frequency satisfies the first sub-harmonic resonance condition.

3.2.1. *Numerical solutions of the RA model*

In order to explore more broadly the behaviour of the RA model and to assess the validity of the saturation criterion equation (3.2), even with strong nonlinear effects, we compute the solutions of (2.12*a*,*b*) for different ω/N_0 ratios and forcing amplitudes F. We choose at $t = 0$ the values, $B(0, \theta) = 0.05$ and $\partial_t B(0, \theta) = 0$. In figure 2, we plot the initial conditions and saturation values in the Mathieu phase diagram. The time evolution of L for a representative case with $F = 1.7$ and $N_0^2/\omega^2 = 3/4$ is also presented.

The parametric instability in the RA model is accompanied by strong oscillations on L and a growth of its mean value. The instability is sub-harmonic as indeed the initial conditions are in the neighbourhood of the first instability tongue. Accordingly, the frequency of oscillation for $L(t)$ with the non-dimensional time is close to ω/N_0 during the growth, corresponding to an oscillation period of $\omega/N_0/2$ for B (not shown). This recovers the classical Faraday phenomenology.

Before discussing the validity of the saturation criterion, equation (3.2), we need to clarify how L_{sat} is evaluated in our simulations. The RA model has no dissipation mechanisms and the final states of L are strongly oscillating. These oscillations are not damped by the phase mixing between the solutions corresponding to different angles θ. They remain at late time even if $L/L_0 \geqslant N_0^2/\omega^2 \mathcal{G}(F)$, i.e. the resonance conditions driving the parametric instability are no longer valid. This interesting effect is the imprint of nonlinearities and is observed also when $F = 0$. Using the multiple scale analysis proposed in § A.2, we can explain this phenomenon as the self-excitation of $\theta = \pi/2$ modes induced by the variations of L. In practice, we simply evaluate L_{sat} by averaging L on the interval $\omega t/N_0 \in [150\ 200]$ on which the simulations seem to have reached a steady oscillating state.

In figure 2, we see that the final states L_{sat} as obtained by the previous procedure are close to the saturation criterion expressed by (3.2) even if the forcing amplitude F is large. All the final states are located in the stable zone of the Mathieu equation. The prediction works better with initial conditions close to the weakly nonlinear analysis case, i.e. in the neighbourhood of the first resonance condition and for small F. Globally, these results bring strong support to the saturation criterion. The next step of our analysis consists then in checking its validity beyond the RA model.

4. Simulations of turbulent mixing driven by parametric forcing

The SHT and MZ equations as introduced in § 2 contain the buoyancy production mechanisms described by the RA model but also dissipation and nonlinear interactions. The question is whether the saturation criterion derived from the simplified RA model can apply to more realistic frameworks. Accordingly, we present in this section different numerical simulations of the SHT and MZ equations with parametric forcing. First, we detail the different simulation set-up. Then we analyse the results.

4.1. *Simulation description*

We provide the different characteristics of SHT and mixing layer simulations dedicated to Faraday instability in the first and the second part of this section respectively.
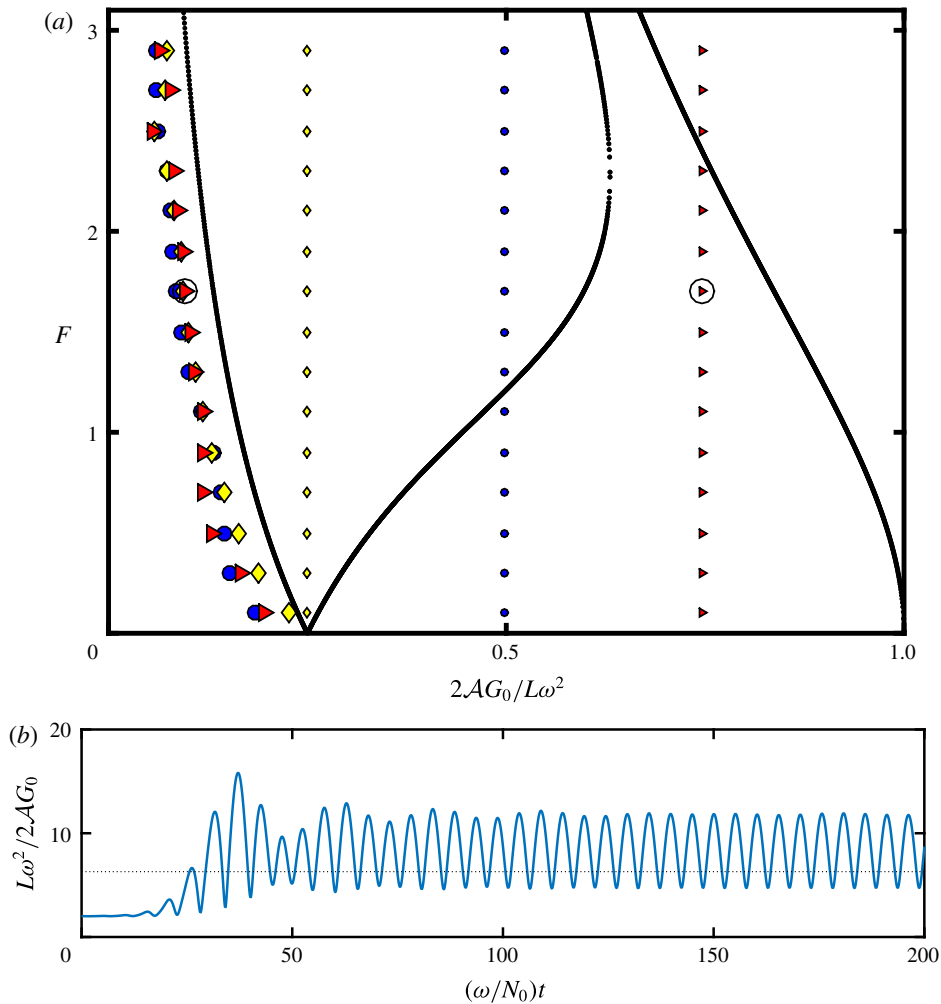
FIGURE 2. (Colour online) (*a*) Representation of the numerical solutions of the RA model in the Mathieu stability diagram. Small symbols: initial conditions. Large symbols: final conditions. Black line: neutral curves of the Mathieu stability diagram. (*b*) Time evolution of the mixing zone width L in the RA model corresponding to $F = 1.7$ and $N_0^2/\omega^2 = 3/4$ (large circle in the Mathieu stability diagram). Dashed line: expected saturation width.

4.1.1. *SHT simulations*

We use for SHT simulations a massively parallel direct numerical simulation (DNS) code based on classical numerical pseudo-spectral methods detailed in Griffond *et al.* (2014). The simulation domain for the turbulent velocity and concentration field is a triply periodic box of size 2π. For convenience, we work with non-dimensional wavenumbers; in particular, $k_{min} = 1$ corresponds to the box size.

Three levels of resolution – small (S) medium (M) and large (L) – with 256^3, 512^3, 1024^3 grid points are performed. The characteristics of the different runs at the initial time are detailed in table 1. The viscosity and diffusion coefficients are taken equal (Schmidt number $= 1$) with values $\mu = \mathcal{D} = 5 \times 10^{-3}$, 2×10^{-3} and 8×10^{-4}

Run	Resolution	$\dfrac{2\mathcal{A}G_0}{L\omega^2}$	F	Fr_I	k_{peak}	n_s
	S 256^3	[0.25 1.25]	[0.1 20]	[0.49 1.1]	9	180
	M 512^3	1.25	[0.2 10]	0.82	15	8
A	M 512^3	[0.062 1.25]	0	[0.82 3.67]	15	7
	L 1024^3	0.25	1.	0.49	4	1
	L 1024^3	0.25	0.3	3.67	30	1
	S 256^3	1.25	1	[0.0548 14.1]	10	9
B	M 512^3	1.25	1	[0.01 1414]	20	13
C	L 1024^3	1.25	1	2.19	40	1

TABLE 1. Non-dimensional parameters at $t = 0$ and number n_s of SHT simulations for the different cases.

respectively for the S, M and L cases. These values ensure that the different scales of the flow are well resolved even during the instability phase (DNS).

The small and medium simulations (S and M) are principally dedicated to the parametric study, in particular to test the initial positions in the Mathieu diagram (Run A) and the influence of initial perturbation intensity (Run B). There is also a special set of M simulations with $F = 0$ (Run A) to ensure that the instability is not triggered when the forcing is switched off. The purpose of large simulations is to investigate turbulent quantities (in particular spectra) during the Faraday instability (Run C) and also to confirm the convergence of results obtained by smaller ones (S and M). Note that large simulations are quite computationally intensive (consuming typically $>5 \times 10^5$ CPU hours spread over 1024 cores) in order to properly capture the instability development (around 20 acceleration periods).

In all our SHT simulations, the mean reduced accelerations and frequencies are fixed respectively at $2\mathcal{A}G_0 = 1$ and $\omega = 2$. The initial mixing width $L(t = 0)$, amplitude F and turbulent quantities may vary in order to explore the phase space. In total, 220 SHT simulations are presented in this work.

The random initial conditions for the concentration c and velocity u_i are isotropic. As a consequence we have $\langle u_i c \rangle = 0$. A narrow wavenumber band centred around k_{peak} is initially excited in Fourier space (peaked spectra) and we specify further the variances $\langle cc \rangle$ and $\langle u_i u_i \rangle$. The choice for k_{peak} is a compromise between the good resolution of the simulations at small scales and keeping a margin for the integral scale to develop freely during the simulations due to nonlinearities. At the end of the simulations, the integral scales usually approach the box size. This effect is difficult to avoid because the Faraday instability needs time to evolve. In Run C, we have tried to reduce these confinement effects by increasing k_{peak} and the resolution. No significant differences concerning the dynamics have been observed compared to less resolved simulations. This is also consistent with results of Thornber (2016) in the different context of decaying turbulence showing that the effects coming from the integral scale confinement appear very lately in spectral simulations.

The flow corresponding to our initial condition with peaked spectra is not turbulent. However, the spectra broaden quite fast due to nonlinear interactions. In addition, the energy brought to the fluctuations by the instability renders it turbulent at later time. Indeed, the turbulent Reynolds number based on kinetic energy, dissipation and viscosity grows due to the instability and reaches values up to $\sim$2000 in L simulations and up to $\sim$500 in S simulations.

Run	Resolution	$\dfrac{2\mathcal{A}G_0}{L\omega^2}$	F	Fr_I	L/L_{box}	n_s
D	S 256^3	[0.05 0.33]	[0.5 5]	[0.05 2] $\times 10^{-2}$	[0.18 0.24]	15
	M 512^3	[0.13 0.96]	[0.4 8.9]	[0.93 6] $\times 10^{-2}$	[0.032 0.1265]	14

TABLE 2. Non-dimensional parameters at $t = 0$ and number n_s of mixing zone simulations.

An important parameter which describes our simulations is the initial Froude number, defined as $Fr_I = (1/2\langle u_i u_i \rangle)^{1/2} k_{peak}/N_0$, giving the ratio between the perturbation and the stratification frequency (see table 1). Here we use a perturbation frequency instead of the classical turbulent one defined from kinetic energy and dissipation since our initial condition is not turbulent. The Froude number expresses whether the simulations are initially buoyancy-driven or ruled by nonlinear effects. This initial Froude number can be easily tuned in our SHT simulations and we show a parametric study of its influence in Run B (discussion postponed to §4.2).

4.1.2. *MZ simulations*

The mixing zone simulations (MZ) are performed with the finite difference parallel code, TURBMIX3D, presented in Poujade & Peybernes (2010), Watteaux (2011). This code solves the Navier–Stokes equations for a binary mixture of two incompressible fluids corresponding in the limit of small Atwood number to (2.1a–c). Here, the Atwood number is chosen as $\mathcal{A} = 10^{-3}$. The computational domain is a cubic box of normalized size $L_{box} = 1$ with periodicity imposed only in the horizontal direction. The mixing zone width L is classically evaluated from the volume fraction profile defined in (2.5).

Simulations with small (S) 256^3 and medium (M) 512^3 resolutions are presented. The viscosity and the diffusivity coefficients are equal (Schmidt number $= 1$) and kept constant but the viscous/diffusive scales are not fully resolved. For this reason, our simulations cannot claim to be DNS but are in the category of implicit large eddy simulations. We motivate this choice to reduce viscous or diffusive effects at large scales which may influence the dynamics of large turbulent structures and the mean density gradient. In particular, we try to have a simulation time $t_{sim} \ll L_{sat}^2/\nu$ to avoid diffusively evolving mixing layers after the Faraday phase. Note that SHT simulations are not limited by this condition.

Another constraint in MZ simulations which is not present in the SHT framework is that the mixing layer must be smaller than the size of the domain $L \leqslant L_{box}$. In practice we try to obtain $L_{sat} \sim 0.5$–$0.6 \times L_{box}$, which seems sufficient to avoid confinement effects as shown by Morgan *et al.* (2017) in the context of Rayleigh–Taylor mixing zones. Also, the use of different resolutions leading to same results guarantees that confinement effects seem very limited in the simulations presented. This leads to the parameters given in table 2 for the 29 MZ simulations.

The initial conditions for our MZ simulations correspond to a developed mixing zone generated by a Rayleigh–Taylor (RT) instability with constant acceleration G_{RT}. The RT mixing phase is initialized using a multi-mode perturbation of the interface. The spectrum for the perturbation height is annular as in Dimonte *et al.* (2004) with wavenumbers $k \in [32\ 64]$ for S simulations, and $k \in [64\ 128]$ for M simulations. Once mixing has been created, the RT phase is halted relatively fast by around the time $\tau = (L_{box}/\mathcal{A}G_{RT})^{1/2}$ corresponding to the nonlinear mixing transition. At this time,

nonlinear coupling and merging processes do not produce fully turbulent mixing (Cook & Dimotakis 2001), but this choice appears as a compromise because of limitations in the final width of L_{sat} due to the top/bottom boundaries of the box. Also due to this constraint, the Froude number Fr_I defined with the integral scale and kinetic energy at the centre of the mixing layer are initially very small.

In summary, we principally dedicate MZ simulations to challenging the validity of the saturation criterion in realistic configurations accounting for inhomogeneous effects neglected by the theory. In complement, the more tractable SHT simulations allow a parametric study of the influence of initial conditions and to investigate the scales of turbulence in more detail.

4.2. *Discussion*

We discuss the results of SHT and MZ simulations together as they exhibit similar phenomena. We first observe the dynamics of both systems during the instability phase before verifying the validity of the saturation criterion equation (3.2). Then we carefully investigate the turbulence characteristics appearing in the systems.

4.2.1. *Time evolution of mixing zone during the instability phase*

To give an overview of the simulation results, we present in figures 3 and 4 the time evolution of L and visualizations of the concentration field at different instants in representative SHT and MZ cases ($F = 1$ and $F = 0.6$ respectively). The evolution of the mixing zone width in both configurations corresponds to the expected scenario, i.e. growth accompanied by oscillations due to the parametric instability followed by a saturation. The oscillations are efficiently damped by dissipative effects when the resonance conditions are no longer fulfilled. This is a striking difference to the RA model.

In both SHT and MZ simulations, the main instability phase is sub-harmonic. The oscillation frequency for L is then ω, and $\omega/2$ for the turbulent quantities. The concentration images at $\omega t = 102$–108 of figure 4 on two successive maxima of L give a good illustration of the phenomenology. This is clearly confirmed by the temporal Fourier transform of $\dot{L}$ provided by figures 3 and 4.

In the SHT case presented in figure 3, the instability begins with a small harmonic phase, as the mixing zone oscillates with a 2ω frequency. The initial parameters for this simulation correspond to the harmonic unstable tongue of the Mathieu diagram. As L grows, the mixing experiences a harmonic/sub-harmonic transition which has important effects on the turbulent structures (this will be discussed in the next section). However, we fail to observe such transitions in our MZ simulations although the phenomenon should be present. It should be stressed that the choice of parameters for MZ simulations is greatly constrained by the size of the computational box contrary to SHT simulations. For instance, if we expect in an MZ simulation a final saturation at $L_{sat}/L_{box} = 0.5$, then the harmonic phase would appear around $L/L_{box} = 0.05$–0.1 for $F = 1$ from the Mathieu phase diagram. The corresponding integral scales ℓ_I are roughly $\ell_I/L_{box} = 0.005$–0.01, and very likely greatly influenced by the numerics and dissipation with our 256^3 or 512^3 resolutions. This might explain why we could not capture the harmonic phase in MZ simulations.

When looking at the time evolution for L in figures 3 and 4, we can observe that the instability does not start initially. This is due to the competition between the dissipation and the turbulent production induced by the parametric forcing. At $\omega t = 0$ the viscous/diffusive dissipation dominates partly because the fluctuation scales
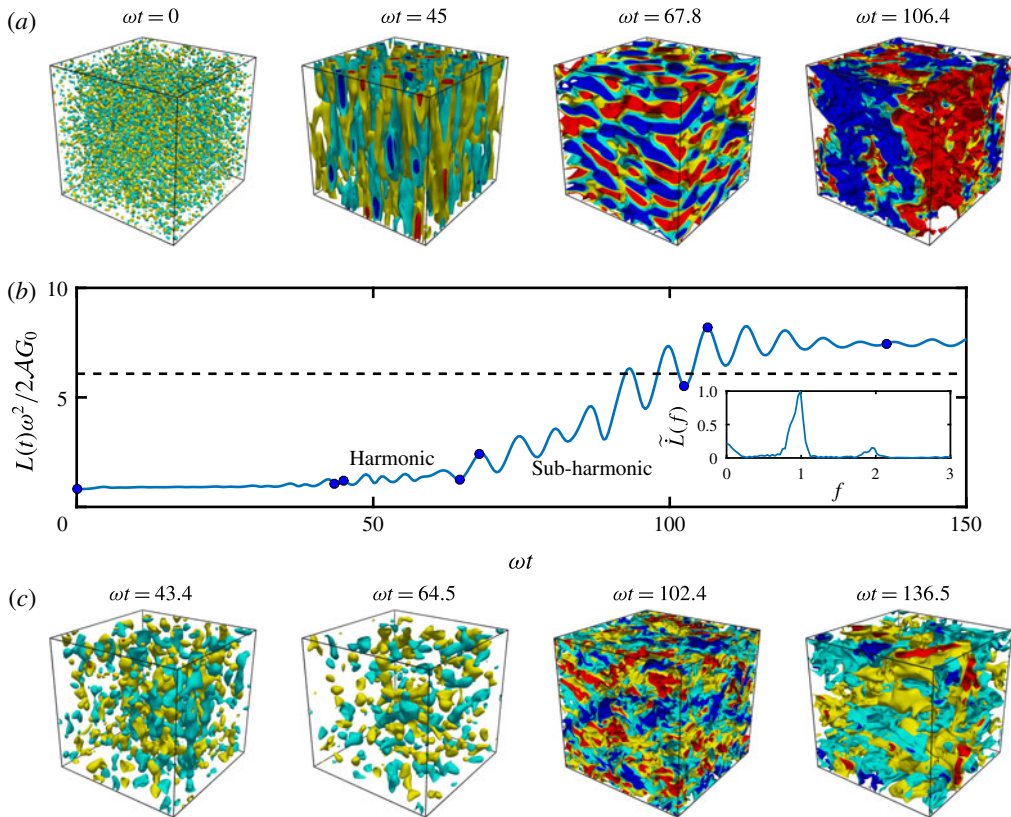
FIGURE 3. (Colour online) Dynamics of Faraday instability for a selected 512^3 SHT simulation with $F = 1$. (*b*) Time evolution of the mixing zone width $L(t)$. Dashed line: predicted saturation. Inset: renormalized time Fourier transform of $\dot{L}$, as a function of the frequency f renormalized by the forcing $\omega/(2\pi)$. Visualization of iso-contours of concentration at different times corresponding to local maxima (*a*) and local minima (*c*). The iso-contour values are $c \in \{-0.2; -0.1; 0.1; 0.2\}$.

are small. At later times, the energy peak is progressively shifted to larger scales where the damping is smaller, leaving the upper hand to the production by parametric forcing. As the energy is gained in the system, the transition to turbulence occurs. It is expected that the viscous/diffusive damping is then replaced by an eddy viscosity term expressing transfer of energy to smaller scales by turbulence. In agreement with these explanations, the mixing width in simulations with high F values increases faster, probably because a higher growth rate of the parametric instability. In contrast, for small values of F the mixing zone slowly evolves without reaching saturation.

4.2.2. *The saturation criterion*

In this section, we specifically discuss the validity of the saturation criterion equation (3.2) in the SHT and MZ simulations. The results are represented in figure 5 on the Mathieu stability diagram containing the initial and final mixing widths for the different simulations.

The initial conditions for the SHT and MZ simulations cover a large domain in the stability diagram with $F \in [0\ 20]$ and $2\mathcal{A}G_0/L\omega^2 \in [0.062\ 1.25]$. In the vast majority of
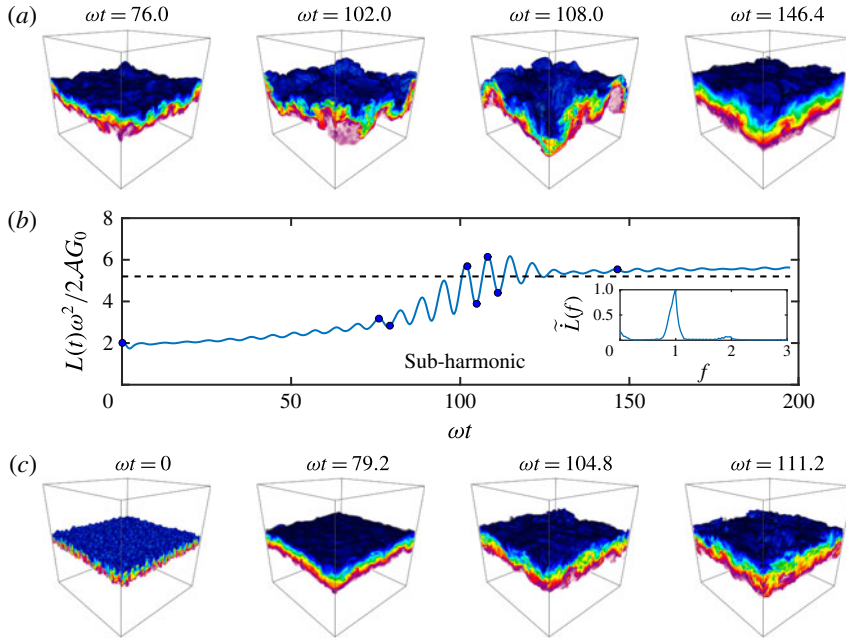
FIGURE 4. (Colour online) Dynamics of Faraday instability for a 512^3 mixing zone simulation with $F = 0.6$. (*b*) Time evolution of the mixing zone width $L(t)$. Dashed line: predicted saturation. Inset: renormalized time Fourier transform of $\dot{L}$, as a function of the frequency f renormalized by the forcing $\omega/(2\pi)$. Visualization of the concentration at different times corresponding to local maxima (*a*) and local minima (*c*). The colour bar varies from $C = 0.99$ (red) to $C = 0.01$ (blue).

the simulations presented, the values of L_{sat} obtained are very close to that predicted by the saturation criterion. This is clear support for the theory developed from the RA model and the main result of this work. In particular, the theory seems valid even in the MZ simulations accounting for the inhomogeneous effects. We also stress that the saturation criterion remains relevant even for large forcing $F \geqslant 1$ where the mixing zone experiences periodically unstable Rayleigh–Taylor phases. As for the RA model, the different final states do not collapse exactly to the transition curve. More precisely, the saturation criterion slightly underestimates L_{sat}, with an error of up to $10\,\%$–$20\,\%$.

Some of the data are far from the predicted values and we try to elucidate this point. For the SHT cases with $F = 0$, the initial and final positions remain nearly the same in the Mathieu stability diagram, confirming if necessary that the simulations with $F \neq 0$ are driven by the parametric instability. However, many SHT simulations with $F \leqslant 0.4$ do not saturate and have a very low growth rate. The neutral stability curve of the RA model in the Mathieu diagram neglects the dissipative mechanisms which level up the instability threshold. The threshold is difficult to determine as it varies with the initial conditions of turbulence. It depends on the viscosity and diffusion coefficient but also on the eddy viscosity expressed by the turbulent kinetic energy and energetic scales of the flow. This explanation supports the Faraday experimental results of Falcón & Fauve (2009), in which a vortex perturbation in the flow increases the instability threshold.

We study in more detail the data corresponding to Run B with $F = 1$ (see table 1) which also differ substantially from the saturation criterion as shown in figure 5.
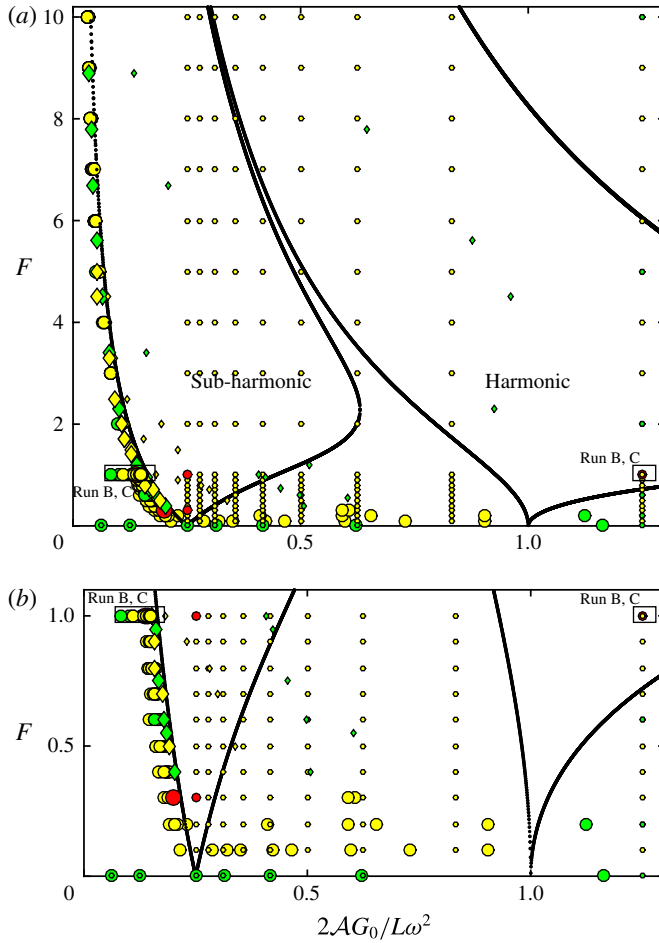
FIGURE 5. (Colour online) Representation of present SHT (circle) and MZ (diamond) simulations in the Mathieu stability diagram. Small symbols: initial conditions. Large symbols: final conditions. Yellow, 256^3; green, 512^3; red, 1024^3. Black line: neutral curves of the Mathieu stability diagram. (*b*) The same as (*a*) but zoomed close to $F = 0$. Initial and final conditions corresponding to Runs B and C are indicated by a rectangle.

Run B simulations have the same initial positions in the Mathieu stability diagram but differ from the initial perturbation intensity expressed by the Froude number Fr_I. In figure 6, we represent the time evolution of L for Run B SHT simulations together with the values L_{sat} as a function of the Froude number. The saturation width L_{sat} is not sensitive to initial conditions as long as the Froude number remains smaller than a limiting value, here around ~ 100. In cases with very large Fr_I, the initial kinetic and potential energies are converted into a large vertical buoyancy flux which enlarges the mixing zone beyond the saturation limit. We try to quantify this more precisely. The gain of potential energy due to the enlargement of a mixing zone with a linear density profile between the initial and saturated final state is

$$\Delta \mathcal{P} = \int_{-\infty}^{+\infty} \frac{\rho_{sat} - \rho_{init}}{\rho_0} G_0 x_3 \, \mathrm{d}x_3 = \frac{1}{12} \mathcal{A} G_0 (L_{sat}^2 - L_{init}^2), \tag{4.1}$$
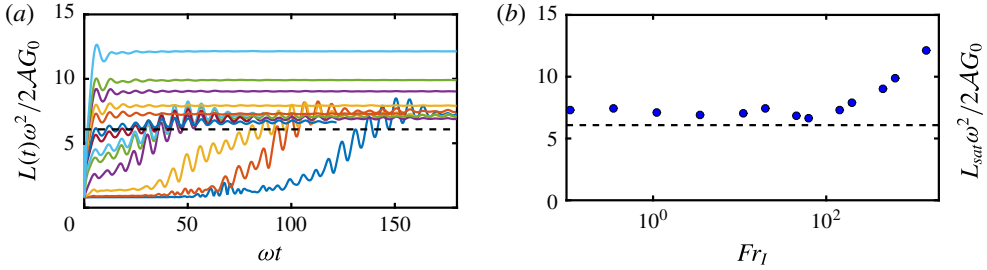
FIGURE 6. (Colour online) Effects of turbulence initial conditions on the saturation width in SHT simulations. Cases correspond to Run B (M) in table 1 and have $F = 1$. (*a*) Time evolution of the mixing zone width. (*b*) Values of the mixing zone saturation width L_{sat} as a function of the initial Froude number defined as $Fr_I = (1/2\langle u_i u_i \rangle)^{1/2} k_{peak}/N_0$. Dashed line: value of the predicted saturation width.

with $\rho_0 = (\rho_1 + \rho_2)/2$. We find that at $Fr_I = 100$, the available initial kinetic energy well exceeds the energy necessary to achieve irreversible mixing corresponding to final state L_{sat} as $K/\Delta\mathcal{P} \sim 100$. As a consequence, a large amount of energy is dissipated into heat at large initial Froude number. This occurs principally at the beginning of the simulations as the initial perturbation is located at small scales in order to allow the growth of the integral scale during the process. Note that similarly to the RA model we can achieve final states well beyond the saturation criterion by imposing a strong initial $\partial_t B$.

To conclude this section, we find that the saturation criterion seems to predict the final states of the mixing zone reasonably well as long as the forcing amplitude is not too small and the perturbation frequency not too big compared to that of the stratification one.

4.2.3. *Turbulence characteristics*

After the overview of SHT and MZ simulations and the discussion concerning the saturation criterion, we now examine the turbulent quantities during the instability phase. The objective is to assess whether the turbulent properties of the mixing are consistent with the theory leading to the saturation criterion. To this end, we present results from the well-resolved SHT simulation Run C (see table 1). The time evolution for L along with the various two-point correlation spectra at different instants are shown in figure 7. We also provide one-point quantities, the Reynolds stress tensor anisotropy, the buoyancy production and dissipation of turbulent kinetic energy in figure 8.

The evolution of the mixing zone width in Run C is quite representative of our simulations, and the saturation obtained is close to the value predicted by criterion equation (3.2). The growth of L and of turbulent quantities such as the kinetic energy $K = \langle u_i u_i \rangle/2$, the variance of concentration $\langle cc \rangle$ and the vertical flux $\langle u_3 c \rangle$ correspond to a sub-harmonic phase. There are also small harmonic modes present at the beginning of the simulations as attested by the temporal spectrum of $\dot{L}$ shown in the inset of figure 7. The oscillations are typical of gravity waves with K and $\langle cc \rangle$ in phase opposition. This point reveals the strong imprint of buoyancy production of kinetic energy defined as $\Pi_B = 2\mathcal{A}G(t)\langle u_3 c \rangle$ and shown in figure 8 which amplitude well exceeds the dissipation ε. This is further confirmed by the small values of the turbulent Froude number defined as $Fr = \varepsilon/NK \sim 0.3$ at the instability apex, here approximately $\omega t = 100$.
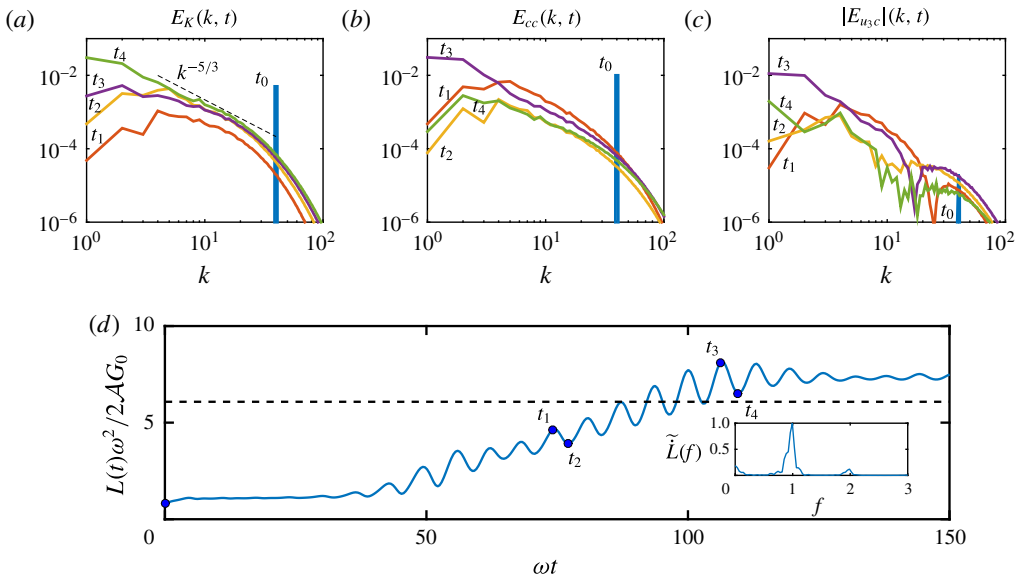
FIGURE 7. (Colour online) (*a–c*) Spectra of kinetic energy $E_K(k, t)$, of scalar $E_{cc}(k, t)$, and of vertical flux $|E_{u_3c}|(k, t)$ at different times. The case corresponds to SHT simulation Run C (L) in table 1. (*d*) Time evolution of the mixing zone width. Blue circles: times corresponding to the different spectra. Dashed line: value of the predicted saturation width. Inset: renormalized time Fourier transform of $\dot{L}$ as a function of the frequency f renormalized by the forcing $\omega/(2\pi)$.

The spectra shown at different times in figure 7 bring more information about the scale-by-scale distribution of energy. The initial peaked spectra rapidly broaden due to nonlinear effects as the instability starts and the wavenumbers corresponding to energetic scales are shifted to the left. This transient phase is accompanied by a strong dissipation as seen in figure 8 for times $\omega t \leqslant 5$. The variation of energy over one oscillation period corresponding to gravity waves phenomena is essentially related to the dynamics of the large scales of turbulence. This supports the analysis provided by the RA model. A change of sign of the concentration flux spectrum is expected during an oscillation period. However, it is interesting to note that at the end of the instability phase, the sign of the concentration flux is not the same for all the scales of the flow. This decorrelation can be simply explained by a different characteristic time between the energy transfer and the parametric forcing. The shift in oscillations between buoyancy production Π_B and dissipation ε in figure 8 can also be attributed to this effect.

At the instability apex corresponding to the last spectra represented, a small inertial zone seems to emerge with a slope close to the classical Kolmogorov scaling law $k^{-5/3}$. It should be stressed, however, that the turbulent Reynolds number remains very modest as already mentioned ($Re = K^2/\varepsilon\nu \sim 2000$). Therefore, the question whether the wave turbulence phenomenology influences the energy transfer in our case remains difficult to analyse due to the low value of the Reynolds number.

In order to pursue this discussion, we study how the structures of turbulence are connected to the flow dynamics. A convenient way to analyse the shapes of turbulent structures, complementary to the visualizations of the concentration field provided by figures 3 and 4 (for the case corresponding to the 1023^3 simulation of figures 7 and 8,
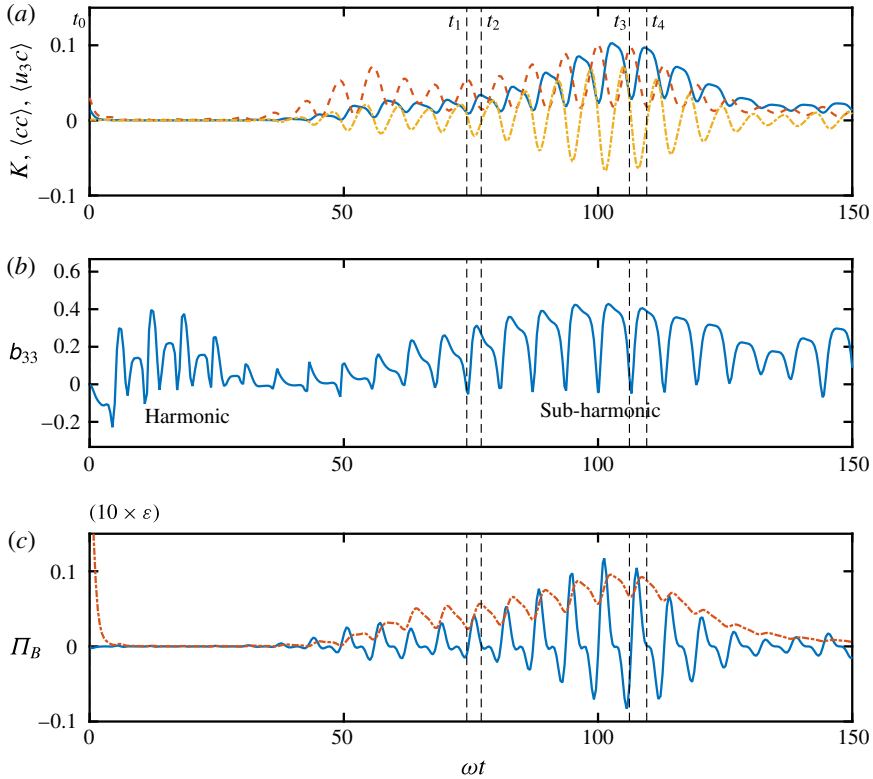
FIGURE 8. (Colour online) (a) Time evolution of kinetic energy K (solid line), scalar variance $\langle cc \rangle$ (dashed line) and vertical buoyancy flux $\langle u_3 c \rangle$ (dot-dashed line). (b) Time evolution of the vertical component of the deviatoric tensor $b_{33} = \langle u_3 u_3 \rangle / \langle u_i u_i \rangle - 1/3$. (c) Buoyancy production Π_B (solid line) and dissipation ε (dashed line) of the turbulent kinetic energy. The case corresponds to SHT simulation Run C (L) in table 1. The specific times corresponding to figure 7 are also indicated.

see also the supplementary movies available at https://doi.org/10.1017/jfm.2017.837), is to measure the anisotropy of the axisymmetric Reynolds stress tensor, represented by its vertical deviatoric component $b_{33} = \langle u_3 u_3 \rangle / \langle u_i u_i \rangle - 1/3$ shown in figure 8. Its time evolution reveals strong oscillations between nearly isotropic states with $b_{33} \simeq 0$, to very anisotropic ones with $b_{33} \simeq 0.2, 0.4$, showing that the kinetic energy is mainly contained in the vertical component. This is clearly the imprint of gravity waves present at large scales and observed in spectra. Accordingly, when the energy is transferred to potential energy, the Reynolds stress tensor returns to isotropy and the velocity field is dominated by the small scales. On the contrary, when the energy is contained in the kinetic energy, the scales and the vertical components of the velocity field grow. As importantly, the harmonic/sub-harmonic then sub-harmonic oscillations of b_{33} follow the evolution of $L(t)$ in the Mathieu phase diagram. Initially, the most amplified gravity waves are harmonic with an orientation along $\theta = \pi/2$ while a narrow band of sub-harmonic modes with small θ is also amplified for $\omega t \in [0\ 40]$. Then, the harmonic modes stabilize, giving the upper hand to the sub-harmonic regime. This transition at $\omega t \in [40\ 50]$ in the simulation corresponds to a sudden decrease of anisotropy as expressed by the b_{33} maxima. The maxima gradually increase for

$\omega t \in [50\ 100]$, which can be explained by the realignment of the most amplified sub-harmonic gravity waves with the vertical direction as L grows. For $\omega t \geqslant 100$ the saturation occurs and we see the return to isotropy of the flow. This scenario can also be observed on the shape of turbulent concentration structures in figure 3. The concentration structures are vertically elongated during the harmonic phase, then suddenly tilted in the harmonic/sub-harmonic transition before straightening up during the final sub-harmonic phase (see also the supplementary movie). Therefore, these observations showing the importance of the nonlinear interaction between gravity waves and the mean density profile support the scenario provided by the RA model.

5. Summary

In this work, we study turbulent mixing zones driven by the Faraday instability which appears at interfaces of miscible fluids, for strong forcing parameter and/or for sufficiently random initial conditions. It is shown that the turbulent mixing zone widths saturate to values predicted from the reduced mean acceleration $2\mathcal{A}G_0$, the oscillation frequency ω and the forcing amplitude F. This saturation criterion, equation (3.2), is simply deduced from the linear stability of each differently oriented gravity waves, parametrically excited by the periodic acceleration inside the mixing zone. We establish the relevance of this approach in the nonlinear regime by introducing the RA model which couples the mixing zone width to the different gravity waves. A multiple scale perturbation analysis close to the first sub-harmonic resonance and the numerical solutions of the RA model attest that the mixing zone width evolves to the first transition curve in the Mathieu stability diagram. The validity of the saturation criterion is further extended by 249 SHT and MZ simulation results, exploring the effects of different parametric forcing and of initial turbulence conditions. As long as the instability is triggered and for not too large initial Froude number, the mixing zone final sizes are predicted by the saturation criterion with a slight underestimation of $0\,\%$–$20\,\%$.

The theory proposed also explains interesting features in the flow. Depending on the initial conditions represented in the Mathieu phase diagram, the instability may be driven by sub-harmonic modes or by a combination of sub-harmonic and harmonic ones. The sub-harmonic regime always prevails at the end of the process as the mixing zone enlarges and saturates. The structure of turbulence is strongly connected to the different phases of the instability. We observe on spectra extracted from the simulations that the large scales are essentially composed of gravity waves. The rapid exchange between kinetic and potential energy explicates the oscillations between nearly isotropic to very anisotropic states populated by large scale structures. Their orientations are thus determined by the most amplified gravity waves, progressively aligning with the vertical direction due to the decrease of the mixing zone natural frequency. In cases where harmonic modes are initially excited, the transition to a purely sub-harmonic regime is accompanied by impressive changes in the turbulence, exhibiting first vertically aligned structures, bending suddenly as the harmonic instability ceases, then progressively realigning with the vertical direction.

These findings can be readily confirmed by experimental studies. They open new possibilities to predict and control the dynamics of turbulent mixing zones.

discussions and remarks concerning the manuscript. The simulations were performed at TGCC, the French computing facility, and the mixing zone images were obtained with the VAPOR visualization software.

Supplementary movies

Supplementary movies are available at https://doi.org/10.1017/jfm.2017.837.

Appendix A. Multiple scale analysis of RA model for $F = 0$

We propose here a perturbation analysis of the RA model, equations (2.12*a,b*), without parametric forcing ($F = 0$). The first part is dedicated to the technical developments leading to the asymptotic expressions for B and L. The method used, while somewhat tedious, presents no difficulties. The second part compares the multiple scale solutions obtained to the numerical solutions of the RA model. We also discuss the effects of nonlinearities in the model.

A.1. *Multiple scale solutions*

The expansion for B follows (3.3) and introducing it in (2.12*b*) gives

$$\Omega(t) = 1 + \varepsilon^2 \Omega^{(0)}(t, \tau) + \cdots . \tag{A 1}$$

The functions $\Omega^{(0)}$ can be expressed by the different terms in the expansion of B but we do not need to express it for the moment. This shows that the nonlinear effects appear at order ε^2 for Ω.

Reintroducing the various expansions in (2.12*a*), we obtain at leading order in ε and ε^2:

$$\partial_{tt} B^{(0)}(t, \tau, \theta) + \sin^2(\theta) B^{(0)}(t, \tau, \theta) = 0, \text{ at order } \varepsilon, \tag{A 2a}$$

$$\partial_{tt} B^{(1)}(t, \tau, \theta) + \sin^2(\theta) B^{(1)}(t, \tau, \theta) = 0, \text{ at order } \varepsilon^2. \tag{A 2b}$$

The solutions can be easily found in the form

$$B^{(0)}(t, \tau, \theta) = a(\tau, \theta) e^{i \sin(\theta) t} + a^*(\tau, \theta) e^{-i \sin(\theta) t}, \tag{A 3a}$$

$$B^{(1)}(t, \tau, \theta) = b(\tau, \theta) e^{i \sin(\theta) t} + b^*(\tau, \theta) e^{-i \sin(\theta) t}, \tag{A 3b}$$

introducing the slow amplitudes $a(\tau, \theta)$ and $b(\tau, \theta)$. Classically in multiple scale analysis, the equations for the amplitudes are obtained by cancelling the secular terms at higher orders.

Before that, we re-inject the solutions for $B^{(0)}$ and $B^{(1)}$ to find a better expression for the frequency Ω. First we have

$$B^2(t, \theta) = \varepsilon^2 (|a|^2(\tau, \theta) + a^2(\tau, \theta) e^{2i \sin(\theta) t}) + \varepsilon^3 (2ab^*(\tau, \theta) + 2ab(\tau, \theta) e^{2i \sin(\theta) t}) + \text{c.c.}, \tag{A 4}$$

with c.c. indicating the complex conjugate of the expression. We now integrate over θ and use a stationary phase approximation to evaluate the integrals of oscillating terms:

$$\int_0^{\pi/2} B^2(t, \theta) \sin(\theta) \, d\theta = 2\varepsilon^2 \Lambda(\tau) + \cdots$$

$$\varepsilon^3 \left(2 \int_0^{\pi} ab^*(\tau, \theta) \sin(\theta) \, d\theta + a^2(\tau, \pi/2) e^{-i\pi/4} \left(\frac{\pi}{\tau} \right)^{1/2} e^{2it} + \text{c.c.} \right), \tag{A 5}$$

with $\Lambda(\tau) = \int_0^\pi |a|^2(\tau, \theta) \sin(\theta) \, \mathrm{d}\theta$. The oscillating terms in (A 4) are put to next order as we use the stationary phase approximation to evaluate integrals over θ. This justifies our choice of $\tau = \varepsilon^2 t$. If we pursue the development, we have the following expression for Ω:

$$\Omega^2(t) = 1 - 2\varepsilon^2 \Lambda(\tau) + \cdots$$
$$-\varepsilon^3 \left(2 \int_0^\pi ab^*(\tau, \theta) \sin(\theta) \, \mathrm{d}\theta + a^2(\tau, \pi/2) \mathrm{e}^{-\mathrm{i}\pi/4} \left(\frac{\pi}{\tau} \right)^{1/2} \mathrm{e}^{2\mathrm{i}t} + \mathrm{c.c.} \right) + \cdots . \quad (A\,6)$$

By taking the time derivative of (A 6), we obtain that the damping coefficient in (2.12a) is $O(\varepsilon^3)$:

$$2 \frac{\dot{\Omega}(t)}{\Omega(t)} = -\varepsilon^3 \left[2\mathrm{i}a^2(\tau, \pi/2) \mathrm{e}^{-\mathrm{i}\pi/4} \left(\frac{\pi}{\tau} \right)^{1/2} \mathrm{e}^{2\mathrm{i}t} + \mathrm{c.c.} \right] + \cdots . \quad (A\,7)$$

At next order ε^3, the equation becomes

$$\partial_{tt} B^{(2)}(t, \tau, \theta) + \sin^2(\theta) B^{(2)}(t, \tau, \theta) = -2\partial_{t\tau} B^{(0)}(t, \tau, \theta) + 2\sin^2(\theta) \Lambda(\tau) B^{(0)}(t, \tau, \theta). \quad (A\,8)$$

The equation for the amplitude a is obtained by cancelling secular terms in $\mathrm{e}^{\mathrm{i}\sin(\theta)t}$ in the right-hand side of (A 8):

$$\partial_\tau a(\tau, \theta) = -\mathrm{i} \sin(\theta) \Lambda(\tau) a(\tau, \theta). \quad (A\,9)$$

Seeking a solution of the form $a(\tau, \theta) = r(\tau, \theta) \mathrm{e}^{\mathrm{i}\alpha(\tau, \theta)}$, we obtain the following system:

$$\partial_\tau r(\tau, \theta) = 0, \quad (A\,10a)$$

$$\partial_\tau \alpha(\tau, \theta) = -\sin(\theta) \int_0^{+\pi} r_0^2(\tau, \theta) \sin \theta \, \mathrm{d}\theta. \quad (A\,10b)$$

Then Λ does not depend on τ, leading to the solution

$$a(\tau, \theta) = a_0(\theta) \mathrm{e}^{-\mathrm{i}\sin(\theta)\Lambda\tau}, \quad (A\,11)$$

such that the complete solution for $B^{(0)}$ is

$$B^{(0)}(t, \tau, \theta) = a_0(\theta) \mathrm{e}^{\mathrm{i}\sin(\theta)(t-\Lambda\tau)} + a_0^*(\theta) \mathrm{e}^{-\mathrm{i}\sin(\theta)(t-\Lambda\tau)}. \quad (A\,12)$$

The next order ε^4 is

$$\partial_{tt} B^{(3)}(t, \tau, \theta) + \sin^2(\theta) B^{(3)}(t, \tau, \theta) = -2\partial_{t\tau} B^{(1)}(t, \tau, \theta) + 2\sin^2(\theta) \Lambda B^{(1)}(t, \tau, \theta) + \cdots$$
$$\sin^2(\theta) \left(2 \int_0^\pi [ab^*(\tau, \theta) + \mathrm{c.c.}] \sin(\theta) \, \mathrm{d}\theta + \left[a^2(\tau, \pi/2) \mathrm{e}^{-\mathrm{i}\pi/4} \left(\frac{\pi}{\tau} \right)^{1/2} \mathrm{e}^{2\mathrm{i}t} + \mathrm{c.c.} \right] \right)$$
$$\times B^{(0)}(t, \tau, \theta) - \left[2\mathrm{i}a^2(\tau, \pi/2) \mathrm{e}^{-\mathrm{i}\pi/4} \left(\frac{\pi}{\tau} \right)^{1/2} \mathrm{e}^{2\mathrm{i}t} + \mathrm{c.c.} \right] \partial_t B^{(0)}(t, \tau, \theta). \quad (A\,13)$$

We write the equation for b by cancelling secular terms in (A 13). For $\theta \neq \pi/2$:

$$2\sin^2(\theta) \Lambda b(\tau, \theta) - 2\mathrm{i} \sin(\theta) \partial_\tau b(\tau, \theta)$$
$$+ 2\sin^2(\theta) \int_0^\pi [ab^*(\tau, \theta) + \mathrm{c.c.}] \sin(\theta) \, \mathrm{d}\theta \, a(\tau, \theta) = 0. \quad (A\,14)$$

In order to solve this equation, we set $b(\tau, \theta) = a(\tau, \theta)s(\tau, \theta)$ leading to

$$-2i\sin(\theta)\partial_\tau s(\tau, \theta) + 2\sin^2(\theta)\int_0^\pi |a_0|^2[s(\tau, \theta) + \text{c.c.}]\sin(\theta)\,d\theta = 0. \quad \text{(A 15)}$$

Separating the real and imaginary part of $s(\tau, \theta)$,

$$\partial_\tau s_r(\tau, \theta) = 0, \quad \text{(A 16a)}$$

$$\partial_\tau s_i(\tau, \theta) + 2\sin(\theta)\int_0^\pi |a_0|^2 s_r(\tau, \theta)\sin(\theta)\,d\theta = 0. \quad \text{(A 16b)}$$

Initially, $b = 0$ and so is s. Therefore this shows that for $\theta \neq \pi/2$, $b(\tau, \theta) = 0$. Then, we turn our attention to the equation for $\theta = \pi/2$:

$$2\Lambda b(\tau, \pi/2) - 2i\partial_\tau b(\tau, \pi/2) + 2\int_0^\pi [ab^*(\tau, \theta) + \text{c.c.}]\sin(\theta)\,d\theta\, a(\tau, \pi/2) + \cdots$$

$$- a(\tau, \pi/2)|a|^2(\tau, \pi/2)e^{-i\pi/4}\left(\frac{\pi}{\tau}\right)^{1/2} = 0. \quad \text{(A 17)}$$

Using $b(\tau, \theta \neq \pi/2) = 0$, we can simplify this expression as

$$2\Lambda b(\tau, \pi/2) - 2i\partial_\tau b(\tau, \pi/2) - a(\tau, \pi/2)|a|^2(\tau, \pi/2)e^{-i\pi/4}\left(\frac{\pi}{\tau}\right)^{1/2} = 0, \quad \text{(A 18)}$$

leading to

$$-2i\partial_\tau s(\tau, \pi/2) - |a_0|^2(\pi/2)e^{-i\pi/4}\left(\frac{\pi}{\tau}\right)^{1/2} = 0, \quad \text{(A 19)}$$

and

$$s(\tau, \pi/2) = |a_0|^2(\pi/2)e^{i\pi/4}(\pi\tau)^{1/2}. \quad \text{(A 20)}$$

Therefore we obtain

$$B(t, \theta) = \varepsilon[a(\tau, \theta)(1 + \varepsilon s(\tau, \theta))e^{i\sin(\theta)t} + \text{c.c.}]. \quad \text{(A 21)}$$

We get the expansion for the mixing zone width as

$$\frac{L(t)}{L_0} = 1 + 2\varepsilon^2\Lambda + \cdots$$

$$\varepsilon^3\left(2\int_0^\pi [ab^*(\tau, \theta) + \text{c.c.}]\sin(\theta)\,d\theta + \left[a^2(\tau, \pi/2)e^{-i\pi/4}\left(\frac{\pi}{\tau}\right)^{1/2}e^{2it} + \text{c.c.}\right]\right) + \cdots$$

$$\varepsilon^4\left(2\left[a^2 s(\tau, \pi/2)e^{-i\pi/4}\left(\frac{\pi}{\tau}\right)^{1/2}e^{2it} + \text{c.c.}\right]\right). \quad \text{(A 22)}$$

Using the expressions for $a(\tau)$ and $s(\tau, \pi/2)$, we obtain a solution for L as a function of the initial conditions:

$$\frac{L(t)}{L_0} = 1 + \varepsilon^2\left(2\Lambda + \varepsilon\left[a_0^2\left(\frac{\pi}{\tau}\right)^{1/2}e^{2it-2i\Lambda\tau-i\pi/4} + \text{c.c.}\right] + 2\varepsilon^2[a_0^2|a_0|^2\pi e^{2it-2i\Lambda\tau} + \text{c.c.}]\right).$$
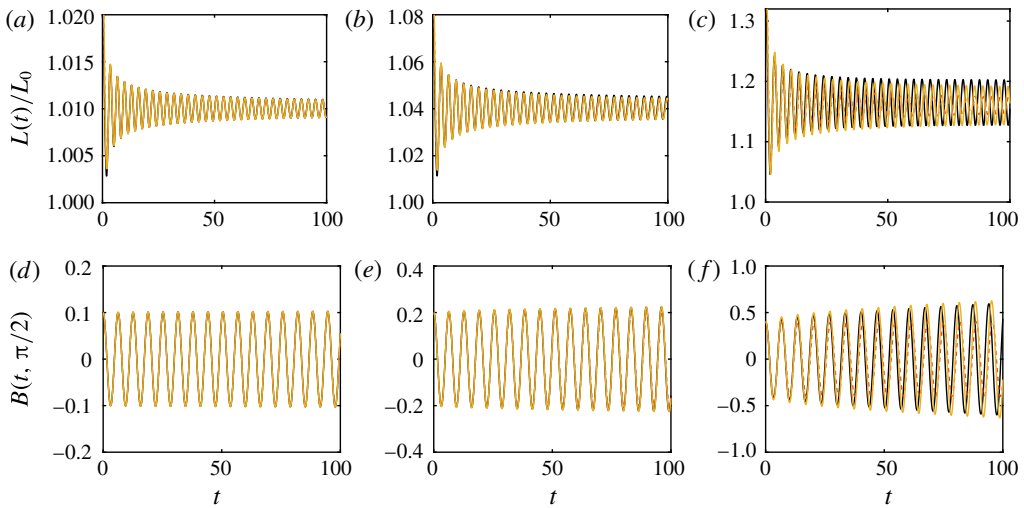
$$\text{(A 23)}$$

FIGURE 9. (Colour online) Time evolution of the mixing zone width L $(a–c)$, and of $B(t, \pi/2)$ $(d–f)$ in the RA model with different initial conditions. (a,d) $B(0, \theta) = 0.1$. (b,e) $B(0, \theta) = 0.2$. (e,f) $B(0, \theta) = 0.4$. Black solid line: numerical solution. Red dashed line: multiple scale analytical solution at order ε^3. Orange solid line: multiple scale analytical solution at order ε^4.

A.2. *Comparison of multiple scale solutions to numerical solutions*

In figure 9, we compare the multiple scale solutions for $L(t)$ and $B(t, \pi/2)$ expressed by (A 23), (A 21) to the numerical solutions of the RA model (2.12*a,b*) with $F = 0$. The multiple scale approximation reproduces well the numerical solutions in the limit of small ε (equivalent to small initial B), and also when the initial perturbation is not so small, as often occurs in perturbation analysis. One can note a small discrepancy in L appearing at short time which comes from the initially divergent stationary phase approximation.

We can now briefly discuss the nonlinear effects in the RA model as revealed by the perturbation analysis. At leading order, the nonlinear term in (2.12*b*) introduces a phase shift but does not modify the oscillation amplitudes. This property is also shared by Duffing oscillators (Bender & Orszag (1978) for instance). The dynamics of L, which depends only on the amplitude of B, is therefore not influenced by this property. However, as shown by figure 9, the mixing zone width L reaches a final state at late time characterized by a finite oscillation amplitude. This is also a nonlinear effect. Indeed in the linear case, the amplitudes for B remain constant and the oscillations for L decrease as $t^{-1/2}$ due to the phase scrambling expressed by the stationary phase approximation. Taking into account nonlinear effects at second order in the multiple scale analysis, the amplitude for $B(t, \pi/2)$ increases as $t^{1/2}$ and compensates for the phase mixing leading to finite amplitudes for L. The sustained oscillations of L can be viewed as a self-excitation of the system with some resemblance to a parametric instability (the growth is algebraic, not exponential). We remark that this effect accompanied by the growth of $B(t, \pi/2)$ favours gravity waves with angles $\theta = \pi/2$ corresponding to elongated structures along the vertical direction.

REFERENCES

AMIROUDINE, S., ZOUESHTIAGH, F. & NARAYANAN, R. 2012 Mixing generated by Faraday instability between miscible liquids. *Phys. Rev.* E **85**, 016326.

ANDREWS, M. J. & SPALDING, D. B. 1990 A simple experiment to investigate two-dimensional mixing by Rayleigh–Taylor instability. *Phys. Fluids* A **2** (6), 922–927.

ARBELL, H. & FINEBERG, J. 2002 Pattern formation in two-frequency forced parametric waves. *Phys. Rev.* E **65**, 036224.

BATCHELOR, G. K., CANUTO, V. M. & CHASNOV, J. R. 1992 Homogeneous buoyancy-generated turbulence. *J. Fluid Mech.* **235**, 349–378.

BATCHELOR, G. K. & NITSCHE, J. M. 1991 Instability of stationary unbounded stratified fluid. *J. Fluid Mech.* **227**, 357–391.

BENDER, C. M. & ORSZAG, S. A. 1978 *Advanced Mathematical Methods for Scientists and Engineers*, McGraw-Hill, reprinted by Springer (1999).

BENIELLI, D. & SOMMERIA, J. 1998 Excitation and breaking of internal gravity waves by parametric instability. *J. Fluid Mech.* **374**, 117–144.

BENJAMIN, T. B. & URSELL, F. 1954 The stability of the plane free surface of a liquid in vertical periodic motion. *Proc. R. Soc. Lond.* A **225** (1163), 505–515.

BINKS, D. & VAN DE WATER, W. 1997 Nonlinear pattern formation of Faraday waves. *Phys. Rev. Lett.* **78**, 4043–4046.

BOSCH, E. & VAN DE WATER, W. 1993 Spatiotemporal intermittency in the Faraday experiment. *Phys. Rev. Lett.* **70**, 3420–3423.

BURLOT, A., GRÉA, B.-J., GODEFERD, F. S., CAMBON, C. & GRIFFOND, J. 2015 Spectral modelling of high Reynolds number unstably stratified homogeneous turbulence. *J. Fluid Mech.* **765**, 17–44.

CHEN, P. & VIÑALS, J. 1999 Amplitude equation and pattern selection in Faraday waves. *Phys. Rev.* E **60**, 559–570.

CHUNG, D. & PULLIN, D. I. 2010 Direct numerical simulation and large-eddy simulation of stationary buoyancy-driven turbulence. *J. Fluid Mech.* **643**, 279–308.

COOK, A. W. & DIMOTAKIS, P. E. 2001 Transition stages of Rayleigh–Taylor instability between miscible fluids. *J. Fluid Mech.* **443**, 69–99.

DIMONTE, G., YOUNGS, D. L., DIMITS, A., WEBER, S., MARINAK, M., WUNSCH, S., GARASI, C., ROBINSON, A., ANDREWS, M. J., RAMAPRABHU, P. *et al.* 2004 A comparative study of the turbulent Rayleigh–Taylor instability using high-resolution three-dimensional numerical simulations: the Alpha-Group collaboration. *Phys. Fluids* **16** (5), 1668–1693.

DIWAKAR, S. V., ZOUESHTIAGH, F., AMIROUDINE, S. & NARAYANAN, R. 2015 The Faraday instability in miscible fluid systems. *Phys. Fluids* **27** (8), 084111.

EDWARDS, W. S. & FAUVE, S. 1994 Patterns and quasi-patterns in the Faraday experiment. *J. Fluid Mech.* **278**, 123–148.

FALCÓN, C. & FAUVE, S. 2009 Wave–vortex interaction. *Phys. Rev.* E **80**, 056213.

FARADAY, M. 1831 On the forms and states of fluids on vibrating elastic surfaces. *Phil. Trans. R. Soc. Lond.* **121**, 319–340.

GAPONENKO, Y. A., TORREGROSA, M., YASNOU, V., MIALDUN, A. & SHEVTSOVA, V. 2015 Dynamics of the interface between miscible liquids subjected to horizontal vibration. *J. Fluid Mech.* **784**, 342–372.

GODRÈCHE, C. & MANNEVILLE, P. (Eds) 2005 *Hydrodynamics and Nonlinear Instabilities*. Cambridge University Press.

GOLLUB, J. P. & RAMSHANKAR, R. 1991 *Spatiotemporal Chaos in Interfacial Waves*, pp. 165–194. Springer.

GRÉA, B.-J. 2013 The rapid acceleration model and the growth rate of a turbulent mixing zone induced by Rayleigh–Taylor instability. *Phys. Fluids* **25** (1), 015118.

GRIFFOND, J., GRÉA, B.-J. & SOULARD, O. 2014 Unstably stratified homogeneous turbulence as a tool for turbulent mixing modeling. *Trans. ASME J. Fluids Engng* **136**, 091201.

HANAZAKI, H. & HUNT, J. C. R. 1996 Linear processes in unsteady stably stratified turbulence. *J. Fluid Mech.* **318**, 303–337.

HUNT, J. C. R. & CARRUTHERS, D. J. 1990 Rapid distortion theory and the problems of turbulence. *J. Fluid Mech.* **212**, 497–532.

JACOBS, J. W., KRIVETS, V. V., TSIKLASHVILI, V. & LIKHACHEV, O. A. 2013 Experiments on the Richtmyer–Meshkov instability with an imposed, random initial perturbation. *Shock Waves* **23**, 407–413.

KUDROLLI, A. & GOLLUB, J. P. 1996 Patterns and spatiotemporal chaos in parametrically forced surface waves: a systematic survey at large aspect ratio. *Physica* D **97** (1), 133–154.

KUMAR, K. & TUCKERMAN, L. S. 1994 Parametric instability of the interface between two fluids. *J. Fluid Mech.* **279**, 49–68.

LIVESCU, D. & RISTORCELLI, J. R. 2007 Buoyancy-driven variable-density turbulence. *J. Fluid Mech.* **591**, 43–71.

MILES, J. & HENDERSON, D. 1990 Parametrically forced surface waves. *Annu. Rev. Fluid Mech.* **22** (1), 143–165.

MORGAN, B. E., OLSON, B. J., WHITE, J. E. & MCFARLAND, J. A. 2017 Self-similarity of a Rayleigh–Taylor mixing layer at low Atwood number with a multimode initial perturbation. *J. Turbul.* **18** (10), 973–999.

MÜLLER, H. W. 1994 Model equations for two-dimensional quasipatterns. *Phys. Rev.* E **49**, 1273–1277.

NAZARENKO, S., KEVLAHAN, N. K.-R. & DUBRULLE, B. 1999 WKB theory for rapid distortion of inhomogeneous turbulence. *J. Fluid Mech.* **390**, 325–348.

POUJADE, O. & PEYBERNES, M. 2010 Growth rate of Rayleigh–Taylor turbulent mixing layers with the foliation approach. *Phys. Rev.* E **81**, 016316.

SIMONELLI, F. & GOLLUB, J. P. 1989 Surface wave mode interactions: effects of symmetry and degeneracy. *J. Fluid Mech.* **199**, 471–494.

SKELDON, A. C. & GUIDOBONI, G. 2007 Pattern selection for Faraday waves in an incompressible viscous fluids. *SIAM J. Appl. Maths* **67**, 1064–1100.

SKELDON, A. C. & RUCKLIDGE, A. M. 2015 Can weakly nonlinear theory explain Faraday wave patterns near onset? *J. Fluid Mech.* **777**, 604–632.

SOULARD, O., GRIFFOND, J. & GRÉA, B.-J. 2015 Large-scale analysis of unconfined self-similar Rayleigh–Taylor turbulence. *Phys. Fluids* **27** (9), 095103.

THORNBER, B. 2016 Impact of domain size and statistical errors in simulations of homogeneous decaying turbulence and the Richtmyer–Meshkov instability. *Phys. Fluids* **28** (4), 045106.

WATTEAUX, R. 2011 Détection des grandes structures turbulentes dans les couches de mélange de type Rayleigh–Taylor en vue de la validation de modèles statistiques turbulents bi-structure. PhD thesis, ENS Cachan.

ZHANG, W. & VIÑALS, J. 1997 Pattern formation in weakly damped parametric surface waves driven by two frequency components. *J. Fluid Mech.* **341**, 225–244.

ZOUESHTIAGH, F., AMIROUDINE, S. & NARAYANAN, R. 2009 Experimental and numerical study of miscible Faraday instability. *J. Fluid Mech.* **628**, 43–55.